Materials Today Bio 22 (2023) 100753

Contents lists available at ScienceDirect

Materials Today Bio

journal homepage: www.journals.elsevier.com/materials-today-bio

A graphene oxide-loaded processed pyritum composite hydrogel for accelerated bone regeneration via mediation of M2 macrophage polarization

Changcan Shi [a,1], Yinting Yu [a,1], Hongjuan Wu [b,c], Huanjin Liu [a], Mengyu Guo [a], Wenxin Wang [a], Dan Wang [d], Chenxu Wei [a], Hao Zhai [e], Guojun Yan [a], Zhipeng Chen [a], Ting Cai [e,*], Weidong Li [a,f,**]

[a] School of Pharmacy, Nanjing University of Chinese Medicine, Nanjing, 210023, China
[b] The First Clinical Medical College, Nanjing University of Chinese Medicine, Nanjing, 210023, China
[c] Department of Pulmonology, Jiangning Hospital of Traditional Chinese Medicine, Nanjing, 211100, China
[d] School of Pharmaceutical Sciences, Tsinghua University, Beijing, 100089, China
[e] State Key Laboratory of Natural Medicines, Department of Pharmaceutics, School of Pharmacy, China Pharmaceutical University, Nanjing, 210009, China
[f] Key Laboratory of State Administration of TCM for Standardization of Chinese Medicine Processing, Nanjing, 210023, China

ARTICLE INFO

Keywords:
Processed pyritum
Metal ions
Hydrogel
Osteoimmunomodulatory effects
Macrophages
Bone regeneration

ABSTRACT

A coordinated interaction between osteogenesis and the osteoimmune microenvironment plays a vital role in regulating bone healing. However, disturbances in the pro- and anti-inflammatory balance hinder the therapeutic advantages of biomaterials. In this study, a novel composite hydrogel was successfully fabricated using graphene oxide (GO)-loaded processed pyritum (PP) in combination with poly(ethylene glycol) diacrylate (PEGDA) and carboxymethyl chitosan (CMC). Subsequently, the immunomodulatory effects and bone regenerative potential of PP/GO@PEGDA/CMC were investigated. The results demonstrated that the PP/GO@PEGDA/CMC hydrogel possessed excellent mechanical properties, swelling capacity, and stability. Moreover, PP/GO@PEGDA/CMC prominently promoted M2 polarization and increased the levels of anti-inflammatory factors (interleukin (IL)-4, IL-10, and transforming growth factor-β). These beneficial effects facilitated the proliferation and osteogenic differentiation of bone marrow mesenchymal stem cells in vitro. Additionally, the in vivo results further verified that the implantation of PP/GO@PEGDA/CMC markedly reduced local inflammation while enhancing bone regeneration at 8 weeks post-implantation. Therefore, the results of this study provide potential therapeutic strategies for bone tissue repair and regeneration by modulating the immune microenvironment.

1. Introduction

Bone-related diseases are a global public health issue, owing to their complexity and specificity. Bone defects, which affect millions of people worldwide, have become major clinical problems. The most common causes of bone defects are accidental injuries, road accidents, skeletal diseases, osteoporosis-related fractures, tumor resection, and aging [1]. Bone autografts and allografts as general treatments for bone repair are expensive procedures, thereby hindering clinical innovation and practical applications. Therefore, there is an urgent need to identify therapeutic treatments and ideal bone biomaterials for in situ bone regeneration.

Bone repair is not accomplished simply by acquiring bone cells from the skeletal system, but by the collaboration of multiple systems [2,3]. Bone regeneration usually involves immunomodulation (suppression or enhancement), vasculogenesis, and osteogenic differentiation. With the ever-increasing use of complex biomaterials in bone tissue engineering, focusing on biomaterial-host inflammatory interactions is of the highest priority [4,5]. The current trend "immune-evasive" biomaterials to "immune-interactive" materials, which will enable their integration and

* Corresponding author.
** Corresponding author. School of pharmacy, Nanjing University of Chinese Medicine, Nanjing, 210023, China.
E-mail addresses: tcai@cpu.edu.cn (T. Cai), liweidong0801@njucm.edu.cn (W. Li).
[1] C. Shi and Y. Yu contributed equally to this work.

https://doi.org/10.1016/j.mtbio.2023.100753
Received 9 February 2023; Received in revised form 27 June 2023; Accepted 28 July 2023
Available online 30 July 2023

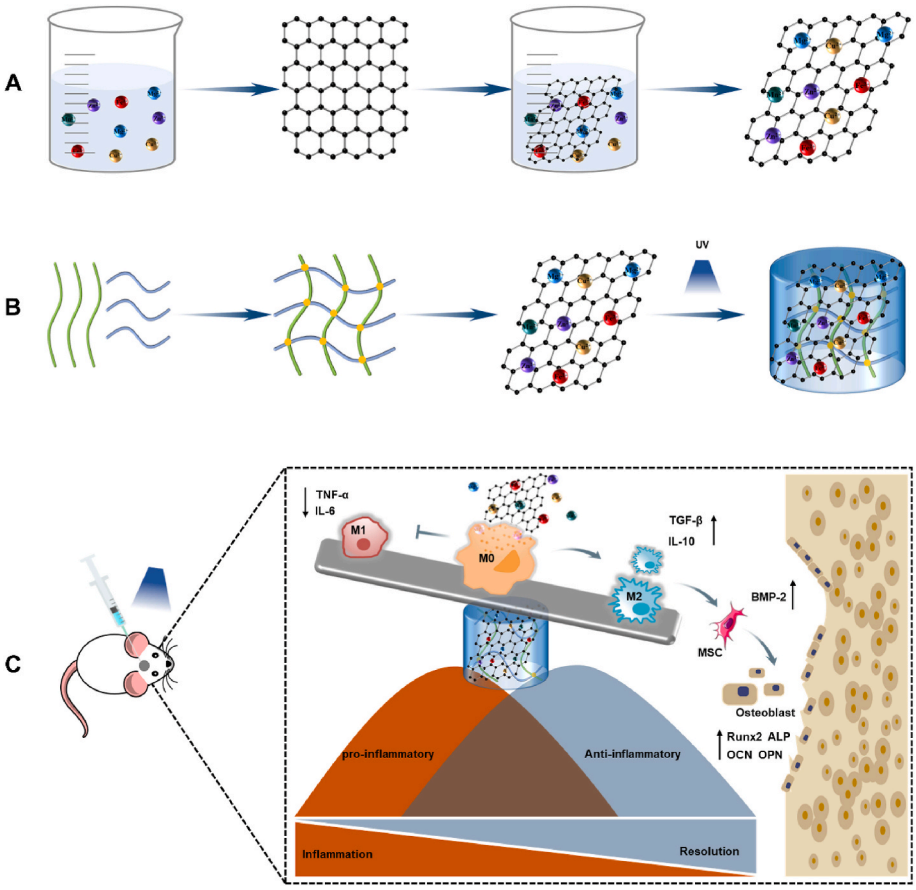

Scheme 1. Schematic diagram of material synthesis and the early bone immune regulation mechanism. (A) Schematic representation of the PP/GO fabrication. (B) Schematic representation of PP/GO@PEGDA/CMC hydrogel preparation. (C) Regulated M1 and M2 macrophage homeostasis promoted osteogenesis and improved bone regeneration applications of the hydrogels.

subsequent tissue repair [6,7]. Consequently, one important consideration in biomaterial design is to create a microenvironment that modulates the inflammatory response and favors tissue repair and regeneration. Therefore, the use of immunomodulation strategies has created the need for biomaterials that can precisely control the biomaterial-host immune response in an appropriate temporal and spatial sequence.

Hydrogels possess 3D network structures formed through cross-linking reactions between hydrophilic polymers, which provide excellent biocompatibility. Thus, they have become attractive biomedical materials for bone tissue engineering [8,9]. New generations of composite hydrogels, similar to drug delivery systems, have been designed for tunable shapes at predesigned sites and are particularly applicable to large-area bone defects [10,11]. However, they still have some drawbacks, such as low mechanical strength and a lack of biological activity [12,13]. Thus, a major challenge is to combine high material strength with fast self-healing ability for bone repair and regeneration [14–16].

Metal ions have been widely accepted as implant materials for the different stages of bone healing [17–19]. Zinc, magnesium, and iron ions are essential elements in bone tissue that participate in many physiological processes of bone metabolism, thereby stimulating osteogenesis and matrix mineralization for bone tissue engineering and regeneration [20,21]. Iron in the mesoporous bioactive glass scaffold stimulates the mitochondrial activity, viability, and differentiation of human bone marrow mesenchymal stem cells (BMSCs), indicating the improved osteoconductivity of the implant [22]. Magnesium is an important intracellular cation that is crucial for bone strength and bone formation [23,24]. It has been proposed that magnesium-based materials are promising candidates for bone repair owing to their ability to stimulate osteoblasts [25,26]. Zinc is an essential trace element with a multitude of physiological functions [27,28]. Furthermore, zinc and zinc alloys are promising biomaterials because they lead to collagen deposition and the mineralization of osteoblasts and antagonize osteoclastogenesis [29].

Pyritum has a good therapeutic reputation with a long history as a traditional Chinese medicine for the treatment of bone fractures [30]. It can be used alone or in combination with other traditional drugs to promote bone formation, heal bone fractures, eliminate blood stagnation, and alleviate pain [31–33]. Pyritum, an isometric crystal ore, mainly contains iron, magnesium, zinc, manganese, and copper. Pyritum can be considered as a natural reservoir of polymetallic elements, which are essential metal ions used for bone repair [34,35]. Moreover, pyritum has been found to be advantageous for facilitating the synthesis of insoluble collagen and promoting the deposition of calcium and phosphorus in animals [36]. A self-assembled chelating peptide hydrogel loaded with an osteogenic metal ion cluster extracted from processed pyritum (PP) decoction has been shown to regulate various genes involved in the process of bone regeneration [37]. However, the low concentrations of the pyritum component in water and the inability to achieve in situ administration result in low therapeutic efficacy, thereby preventing wide clinical applications. Hence, its therapeutic potential is yet to be explored.

Graphene oxide (GO), with a single layer of sp^2-bonded carbon atoms, is regarded as a promising nanomaterial owing to its excellent bioactive properties, mechanical strength, and adsorption capacity [38–41]. Thus, GO should be a favorable additive to enhance the mechanical strength of the hydrogels. Moreover, it is known that GO is an ideal candidate for a controlled release carrier of various metal ions for bone repair and regeneration. Furthermore, GO sheets of differing

lateral dimensions are effectively degraded by neutrophils and the degradation products are non-cytotoxic and do not elicit any DNA damage [42,43].

In this study, a design strategy using a novel mineral–organic nano-compound hydrogel for bone tissue regeneration applications, inspired by the good therapeutic reputation of pyritum in traditional medicine, was proposed. As shown in Scheme 1, PP-enriched GO was used as a drug delivery system to fabricate a nano-compound hydrogel that integrated carboxymethyl chitosan (CMC) with poly(ethylene glycol) diacrylate (PEGDA). The cytocompatibility and osteoimmunomodulatory properties of these hydrogels were systematically investigated in vitro. More importantly, the results of this study demonstrated that the mineral–organic nano-compound hydrogel significantly mediated the early immune response from the pro-inflammatory M1 phenotype to the anti-inflammatory M2 phenotype. Finally, the regenerative potential of the nanocomposite hydrogels in a critical-sized rat calvarial defect model was investigated.

2. Materials and methods

2.1. Materials

PP was provided by the Kangmei Pharmaceutical Co. Ltd. (Guangdong, China).PEGDA (containing 400–600 ppm MEHQ stabilizer) was purchased from the Shanghai Yuanye Biotechnology Co. Ltd. (China). CMC was purchased from the Zhejiang Aoxing Biotechnology Co. Ltd. (China). GO was obtained from the Xianfeng Nanomaterials Technology Co. Ltd. (Jiangsu, China). 2-Hydroxy-4-(2-hydroxyethoxy)-2-methylpropiophenone (Photoinitiator 2959) was purchased from Aladdin Reagent (Shanghai, China). Interleukin (IL)-6, IL-4, IL-10, transforming growth factor-β (TGF-β), and tumor necrosis factor-α (TNF-α) ELISA kits were purchased from YIFEIXUE BIOTECH (Nanjing, China). FITC-conjugated anti-CD86, PE-conjugated anti-CD206, recombinant *anti*-iNOS, *anti*-osteocalcin (OCN), and anti-alkaline phosphatase (ALP) antibodies were purchased from Thermo Fisher Scientific (Waltham, MA, USA). CD68 rabbit polyclonal, bone morphogenetic protein-2 (BMP-2) polyclonal, runt-related transcription factor 2 (RUNX2), and osteopontin (OPN) polyclonal antibodies were purchased from AiFang Biological (Hunan, China). Osteogenic inducting fluid was purchased from Procell (Wuhan, China). ALP Color Development Kit and Alizarin red S (ARS) kit were purchased from Beyotime (Shanghai China).

2.2. Design and fabrication of hydrogels

2.2.1. Preparation of the GO@PEGDA/CMC hydrogel

To obtain GO solution, GO power was dissolved in deionized water under ultrasonication for 2 h. Phosphate-buffered saline (PBS; pH 7.2–7.4) was used to obtain a CMC solution and PEGDA solution. Photoinitiator 2959 was added to the PEGDA solution at a concentration of 0.4% (*w/v*). After full oscillation, the solution was mixed with the CMC solution (*v/v*; 1/2) to blend evenly, resulting in a final PEGDA concentration of 4% (*w/v*) and CMC concentration of 2% (*w/v*). A standard GO@PEGDA/CMC hydrogel was fabricated by dispersing GO in a PEGDA/CMC solution and then cross-linking under 365 nm UV light for 2 min. The final concentration of GO in the hydrogel was 0.1 mg/mL.

2.2.2. Preparation of the PP/GO@PEGDA/CMC hydrogel

To obtain PP/GO, static adsorption was performed as follows: GO powder and PP were mixed and shaken at 150 rpm for 48 h at 25 °C (*w/v*: 1/1). After centrifugation at 3000 rpm for 10 min, the supernatant was discarded and the insoluble substance was dried at 50 °C for 8 h. The solid particles were dissolved in deionized water under ultrasonication for 2 h to obtain the PP/GO solution. The preparation process of PEGDA and CMC solutions was consistent with that of PEGDA and CMC solutions in section ***2.2.1***. A standard PP/GO@PEGDA/CMC hydrogel was fabricated by dispersing PP/GO in a PEGDA/CMC solution and then crosslinking under 365 nm UV light for 2 min. The final concentration of GO was 0.1 mg/mL, and the final concentration of PP was 17.5 μg/mL. The mass of PP was expressed as the mass of the iron ion.

2.3. Characterization of hydrogels

2.3.1. Apparent morphology of hydrogels

To observe the microstructure of the hydrogels, lyophilized samples were characterized by field emission scanning electron microscopy (SEM, Quanta FEG 250) with an accelerating voltage of 20 kV. To improve the conductivity of the samples, a sputter coater (LEICA EM SCD 500) was used to spray gold on the samples (16 mA, gold-sprayed Pt, 120 s).

2.3.2. Rheological measurements

The dynamic rheological properties of three hydrogels (PEGDA/CMC, GO@PEGDA/CMC, and PP/GO@PEGDA/CMC) were measured at 25 °C using an MRS60 rheometer (Thermo Fisher, Germany). The hydrogel was positioned into a 0.4 mm gap between the plates, and the normal force was adjusted to zero. Strain amplitude sweeps (0.01–100%) were conducted to ascertain the linear viscoelasticity region. Then storage modulus G' and loss modulus G'' of the hydrogels were detected under the frequency range varying from 0.10 Hz to 10.00 Hz at 25 °C and 15 Pa. Finally, the loss factor was then obtained.

2.3.3. Mechanical testing

To measure the mechanical properties, hydrogels were tested using a low-load tension-compression testing machine (Shimadzu-EZ LX, Japan) at a working temperature of 25 °C. Three hydrogels, PEGDA/CMC, GO@PEGDA/CMC, and PP/GO@PEGDA/CMC, were tested. During the compression test, the samples were compressed using a circular indenter with a strain rate of 1.0 mm min^{-1} until they broke. The maximum compressive strength of the hydrogels was recorded. Three parallel samples were used in this experiment.

2.3.4. Water content and swelling ratio of the hydrogels

The hydrogels were equilibrated in a PBS (pH 7.2–7.4) solution for 24 h, and the excess solution on the surface was absorbed using qualitative filter paper. Subsequently, the wet hydrogels were lyophilized for 24 h to obtain dried gels. The water content of the hydrogels was determined using **Equation (1)**:

$$HW(\%) = \left(\frac{W_1 - W_2}{W_1}\right) \times 100 \quad (1)$$

where W_1 and W_2 denote the weight of wet and dried hydrogels, respectively.

The hydrogels were swollen in a PBS solution at 37 °C. Subsequently, the swelling was measured by weighing the hydrogels at time intervals (0.5, 1, 2, 3, 5, 9, 12, 24, and 48 h). The swelling efficiency of the developed hydrogels was quantified using **Equation (2)**:

$$RSW(\%) = \left(\frac{M_i - M_0}{M_0}\right) \times 100 \quad (2)$$

where M_0 and M_i denote the weight of initial and swollen hydrogels, respectively.

2.3.5. Degradation assay in vitro

The degradation behavior of the hydrogels was analyzed in PBS (pH 7.2–7.4) at 37 °C, 150 rpm. Briefly, hydrogels of known weights were dipped into PBS (pH 7.2–7.4) for a fixed time. The solution was collected and replaced during specific periods. The collected solution was weighed after lyophilization. The mass of the lyophilized solute corresponding to the same volume of PBS was subtracted according to the volume of the collected solution. Then, the daily degradation mass of the hydrogel was obtained. The degradation rate was expressed as the daily

cumulative mass.

2.3.6. FTIR spectra analysis

The functional groups in the three hydrogels were analyzed by an FTIR analyzer (Bruker, Germany) in the regions of 400–4000 cm^{-1}.

2.3.7. EDS analysis

Each element emits characteristic X-rays when excited, and these X-rays have different frequencies. An energy-dispersive spectrometer (EDAX, USA) was used to qualitatively analyze the samples.

2.3.8. Release analysis of elements

Firstly, the concentration of various elements in the PP decoction (1 g/mL) was detected by ICP-MS (Analytik Jena AG, Germany). Then, to measure the content of metal ions released, the samples were detected at different times by ICP-MS. The hydrogels were completely immersed in deionized water at 37 °C and shaken at 120 rpm to accelerate their release. The solution was collected at specified time points and passed through a 0.45 μm filter membrane. The filtrate was then loaded into the ICP-MS to measure the content of metal ions released over time, and a line chart of the release of each element was drawn. The ICP-MS detection method settings were as follows: flow parameters ($L{\cdot}min^{-1}$): plasma flow, 9.0; auxiliary flow, 1.50; sheath gas, 0.00; nebulizer flow, 1.00; sampling depth, 5 mm; RF powder (kW), 1.15; pump rate (rpm), 16; iCRC ($mL{\cdot}min^{-1}$): skimmer gas source, H_2; skimmer flow, 90.

2.4. In vitro cell experiments

2.4.1. Cell culture

Raw 264.7 macrophages were maintained in a growth medium (DMEM with 10% FBS and 1% P/S) and incubated at 37 °C in a humid environment containing 5% CO_2. The cell densities were different according to the experimental requirements. The cells were prepared and seeded in 96-well, 24-well, and 6-well cell plates. Cells in good condition were selected for the following study after receiving the base treatment for the specified time.

2.4.2. Preparation of hydrogel-conditioned medium

The PEGDA/CMC, GO@PEGDA/CMC, and PP/GO@PEGDA/CMC hydrogels were first rinsed with PBS solution. Subsequently, they were placed into the growth medium and extracted for 48 h at 37°Cand 150 rpm. The extract was filtered through a 0.22 μm sterile membrane to obtain the hydrogel-conditioned medium.

2.4.3. Cell viability and proliferation

A CCK-8 assay was used to evaluate the proliferation of Raw 264.7 macrophages. Cells were inoculated in 96-well plates at a concentration of 1.5×10^4/well. After cell adhesion for 8 h, the medium was replaced with hydrogel-conditioned medium to culture the cells for 48 h. Then, 100 μL of hydrogel-conditioned medium was added to each well. After being washed with PBS, the cells were treated with 10% CCK-8 solution in DMEM at 37 °C for 1 h, taking care not to generate air bubbles during the procedure. Absorbance was measured at a wavelength of 450 nm.

Cells were seeded into a 48-well plate at a density of 5×10^4/well and cultured for 24 h. The growth medium was then replaced with hydrogel-conditioned medium to culture the cells for an additional 48 h. Next, 500 μL of hydrogel-conditioned medium was added to each well. The supernatant was discarded, the cells were washed with PBS, and the calcein/PI working solution was added according to the manufacturer's instructions. After staining in the dark at 37 °C for 30 min, the cells were captured and photographed under an ortho-fluorescent microscope (NIKON ECLIPSE C1, Nikon, Japan).

2.4.4. ELISA analysis

ELISA kits were used to evaluate macrophage polarization in vitro. In short, cells were cultured in a conditioned medium for 48 h, then the supernatant was collected and centrifuged at 1000×*g* for 20 min. The inflammatory factors (TNF-α, IL-6, IL-10 and TGF-β) levels were detected at 450 nm according to the manufacturer's instructions.

2.4.5. Flow cytometry analysis

Flow cytometry (FCM) was used to assess macrophage polarization. Due to the immune responses usually occurring in the early stage, Raw 264.7 macrophages co-cultured with hydrogels for 48 h were collected. Cells were seeded in 6-well plates at a density of 1×10^6/well. After being cultured with the hydrogels for 48 h, the cells were harvested. Staining was performed according to the manufacturer's instructions and the cells were collected and tested. The expression levels of CD86 and CD206 were analyzed.

2.4.6. Immunofluorescence staining

The Raw 264.7 macrophages were seeded onto round cell slides at a density of 5×10^5 cells per well and placed at the bottom of a 24-well plate. After cell adhesion for 2 h, fresh medium containing hydrogels was added to the plate and then cultured at 37 °C for 48 h. Cell slides were collected to evaluate the macrophage phenotype through immunofluorescence staining with iNOS and CD206. The slides were observed and photographed under an ortho-fluorescent microscope (NIKON ECLIPSE C1, Nikon, Japan).

2.4.7. Osteogenic differentiation assay

To determine the effects of macrophages treated with different hydrogel-conditioned media on the osteogenic differentiation of BMSCs, a Transwell co-culture system was used (Fig. 5C). Raw 264.7 macrophages were seeded on Transwell inserts containing 0.4 μm pores in each well at a density of 1×10^5 cells per well in 6-well plates. Then they were treated with different hydrogel-conditioned media. BMSCs were seeded in flat-bottom 6-well Transwell plates at a density of 1×10^6 cells per well. BMSCs and macrophages were seeded in a Transwell co-culture system. After 48 h of incubation, the growth culture medium was replaced with osteogenic inducting fluid. ALP staining was detected on day 7. After 2 weeks of induction, calcium deposition was assessed using ARS staining. Total RNA was harvested after 7 days of co-culture to determine the expression of osteogenesis-related genes using RT-qPCR.

2.5. In vivo animal experiments

2.5.1. Construction of the calvarial defect model

All animal experiments strictly abided to the Animal Experiment Ethics Committee of Nanjing University of Traditional Chinese Medicine according to the guidelines for animal care, use, and euthanasia of rats (approval no. 202202A024). Sprague–Dawley rats (200 ± 50 g, male) were used to establish a bilateral skull defect model to assess the regenerative capacity of composite hydrogels. Briefly, the rats were anesthetized and their heads were disinfected with iodine disinfectant after depilation. A 1.5 cm incision was made in the center of the head to expose the cranium, the soft tissue attached to the bone was fully dissected, and two 4 mm-diameter defects were made using a surgical trephine drill. The wound was flushed with a large amount of sterile saline for cooling. Each defect was cleaned and hydrogels were implanted in them. After 1 min of UV irradiation, the periosteum and skin were intermittently sutured with 3-0 sutures. Following surgery, all rats were monitored until sternal recumbency was regained. Penicillin was injected intramuscularly in all rats at a concentration of 800,000 $units{\cdot}kg^{-1}$ for 3 days to avoid infection. Herein, a total of 32 rats were divided into four groups (n = 8) as follows: (1) Control group with PBS implantation, (2) PEGDA/CMC group, (3) GO@PEGDA/CMC group, and (4) PP/GO@PEGDA/CMC group. The rats were euthanized at 3 days, 7 days, 4 weeks, and 8 weeks after implantation, respectively. The skulls were harvested and fixed in 4% paraformaldehyde for further analysis.

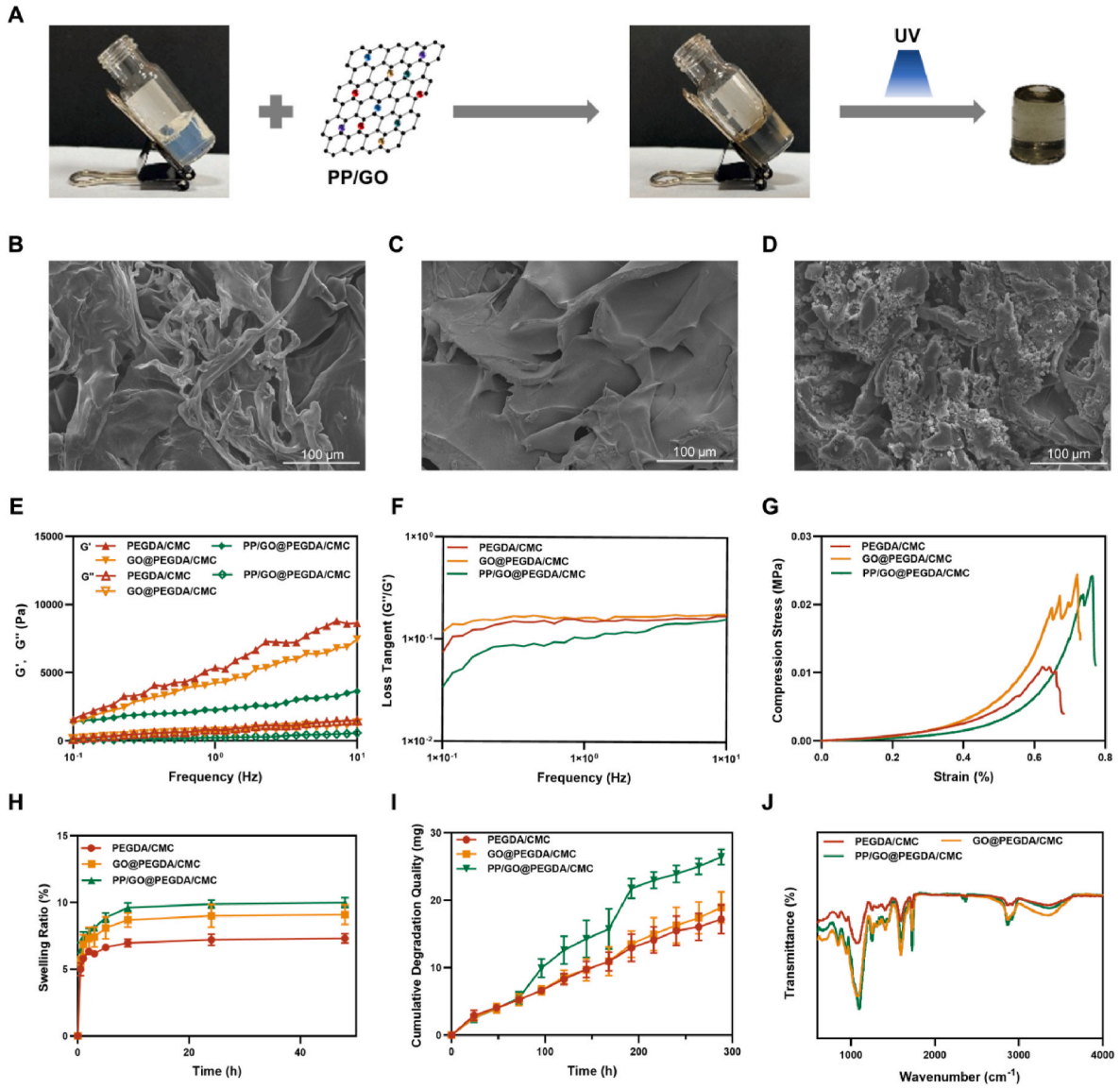

Fig. 1. Synthesis process and characterization of hydrogels. (A) The preparation process of the PP/GO@PEGDA/CMC hydrogel. SEM images of the microstructures of (B) PEGDA/CMC hydrogel, (C) GO@PEGDA/CMC hydrogel, and (D) PP/GO@PEGDA/CMC hydrogel. (E) Storage modulus (G′) and loss modulus (G″) of various hydrogels. (F) Loss tangent (G′′/G′) of various hydrogels. (G) Representative compression stress-strain curves of the PEGDA/CMC, GO@PEGDA/CMC, and PP/GO@PEGDA/CMC hydrogels. (H) Swelling characteristics of the PEGDA/CMC, GO@PEGDA/CMC, and PP/GO@PEGDA/CMC hydrogels (mean ± SD, n = 3). (I) Degradation of the PEGDA/CMC, GO@PEGDA/CMC, and PP/GO@PEGDA/CMC hydrogels in vitro (mean ± SD, n = 3). (J) FTIR spectra of the PEGDA/CMC, GO@PEGDA/CMC, and PP/GO@PEGDA/CMC hydrogels.

2.5.2. Micro-CT analysis

To evaluate bone reconstruction at the calvarial defect sites, a high-resolution micro-CT scanner (Germany, SkyScan1176, Bruker) with 1 mm Al filtration (385 μA, 65 kV) was used to scan the samples. The exposure time was 340 ms, and 246 images were acquired. Version 1.1 was used to obtain the first step of the reconstructed data. The resolution was 17.76 μm for the image pixel size and the voxel size of the reconstruction. DataViewer software was used to reconstruct images of interest. After obtaining the three-dimensional (3D) reconstruction results, CTAn software was used for deep analysis. The analyses included bone volume (BV), bone mineral density (BMD), bone volume fraction (BV/TV), trabecular number (Tb.N), and trabecular thickness (Tb.Th). A 3D model of the skull and a three-dimensional model of the new bone were constructed using CTvox software.

2.5.3. Histological evaluation

After CT scanning, the skull samples were decalcified in 10% EDTA for 60 days with solution replacement every 2 days. Thereafter, the decalcified samples were embedded in paraffin and serial sections (3 μm thickness) and prepared using a pathology slicer. Immunofluorescence staining for CD68 and CD206 was performed to evaluate macrophage polarization and function. Hematoxylin and eosin (HE) and Masson's staining were performed to observe new bone reconstructions. In addition, immunofluorescence staining for BMP-2, RUNX-2, ALP, OCN, and OPN was performed. Images were obtained using an inverted fluorescence microscope (FluoView 500; Olympus, Tokyo, Japan). The mean integral optical density (IOD) values of the different fluorescence signals were detected using Image Pro Plus software (version 6.0) to evaluate the expression of proteins.

2.5.4. Analysis of serum immune factors

The levels of immune factors (TNF-α, IL-6, IL-4, and IL-10) in serum samples were measured using the TNF-α, IL-6, IL-4, and IL-10 ELISA Kits. All steps were performed according to the manufacturer's instructions.

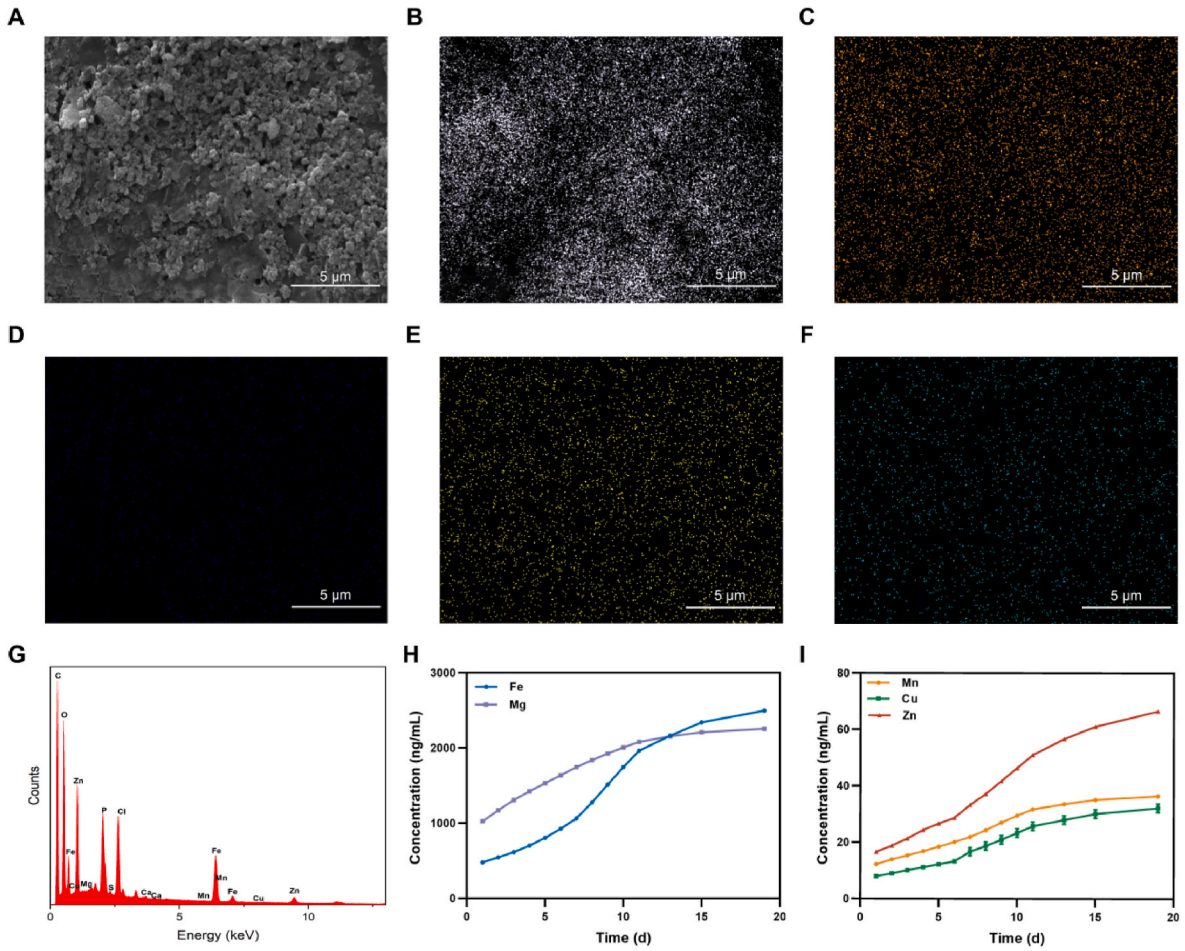

Fig. 2. Identification of metal ions and ICP-MS analysis. EDS mapping for (A) the area analyzed, (B) iron, (C) magnesium, (D) copper, (E) zinc, and (F) manganese; the spectrum with major peaks is shown in (G). (H) Release profiles of iron and magnesium ions from PEGDA/CMC wrapped with PP/GO (mean ± SD, n = 3). (I) Release profiles of copper, zinc, and manganese ions from PEGDA/CMC wrapped with PP/GO (mean ± SD, n = 3).

2.6. Statistical analysis

All quantitative data in this study are presented as the mean ± standard deviation (SD), and each experiment was performed with at least three replicates. Statistical significance was determined using one- or two-way ANOVA using GraphPad Prism 8.4.2 software. $*p < 0.05$, $**p < 0.01$, and $***p < 0.001$ indicated a statistically significant difference.

3. Results and discussion

3.1. Synthesis and characterization of PP/GO@PEGDA/CMC hydrogels

According to previous studies, PP provides active factors because the metal ions in PP are effective in healing bone defects [33]. GO sheets with carboxyl, epoxy, and hydroxyl groups can be effective in the adsorption of metal ions. Adsorption forces are mainly derived from electrostatic interactions, complexation, and cationic-π bond interactions [44,45]. In this study, the effect of GO sheets on metal ion (iron, magnesium, copper, zinc, and manganese ions) adsorption capacities was studied using a PP decoction. Adsorption experiments showed that the GO sheets had a good adsorption capacity for metal ions. The formation of the PP/GO complex was a unique advantage for the hydrogels. The process was simple but effective, and tedious procedures were avoided. PP/GO@PEGDA/CMC hydrogels were prepared by dispersing the PP/GO solution into the PEGDA/CMC network. The preparation process for the PP/GO@PEGDA/CMC hydrogel is shown in Fig. 1A. The PP/GO@PEGDA/CMC composite hydrogel was light gray and contained no obvious impurities.

As shown by SEM, the hydrogels displayed 3D architectures with a diameter of 100 μm. The PEGDA/CMC hydrogel had a smooth surface (Fig. 1B). There was edge sharpening, wall thickening, and sheet-like morphology in the GO@PEGDA/CMC hydrogel (Fig. 1C). The PP/GO@PEGDA/CMC hydrogel had a more complicated 3D architecture with particles of varying sizes in the voids (Fig. 1D). The prepared hydrogels were evaluated by rheological tests and mechanical measurements. The viscous behavior of the hydrogels was slightly enhanced; however, the elastic behavior was significantly enhanced after the addition of GO (Fig. 1E). Interestingly, the PP/GO@PEGDA/CMC hydrogel possessed a smaller loss tangent, which was independent of the frequency in the range of 0.10–10.00 Hz (Fig. 1F). The results showed that the comprehensive properties of the original PEGDA/CMC hydrogel crosslinked network were enhanced by the PP/GO. Briefly, the PP/GO@PEGDA/CMC hydrogel could withstand large deformations owing to its good elasticity and high resistance. Likewise, under compressive loading (Fig. 1G and Fig. S1), the PP/GO@PEGDA/CMC hydrogel exhibited a maximum strength of 24.1 kPa and a large deformation capacity of 76.3%. However, the maximum strength of the PEGDA/CMC hydrogel was approximately 10.8 kPa, the critical strength it could withstand was 7.0 kPa, and the maximum strain was 62.1%. It fractured before the strain reached 76.3%. These results were consistent with the rheological test results, indicating that the mechanical properties of the hydrogels were greatly improved after the addition of GO, which could meet the requirements of cranial repair.

Table 1
Concentration of various elements in the PP decoction (1 g/mL).

Element name	Content (μg/mL)
Fe	4172.04
Mg	180.00
Zn	7.55
Mn	16.33
Cu	0.08

In this study, the water uptake of the PP/GO@PEGDA/CMC hydrogel was highest. The swelling rate curve in Fig. 1H shows that the freeze-dried hydrogels swelled rapidly at the beginning. However, the swelling ability began to slow and finally reached swelling equilibrium over time. The swelling performances of the PEGDA/CMC and GO@PEGDA/CMC hydrogels were 7.3 ± 0.3 and 9.1 ± 0.7, respectively. Compared with other hydrogels, the PP/GO@PEGDA/CMC hydrogels had the best swelling performance (10.0 ± 0.4). The swelling and degradation properties of hydrogels are considered major parameters in tissue engineering because they are closely related to the absorption of nutrients, transport, and excretion of metabolites in vivo. The in vitro degradation results showed that the hydrogel gradually degraded as a function of time (Fig. 1I). The PP/GO@PEGDA/CMC hydrogel was degraded at a higher rate than the PEGDA/CMC and GO@PEGDA/CMC hydrogels. At day 12, all types of hydrogels were completely degraded. These results indicated that the adsorption of metal ions by GO resulted in a larger pore structure of the hydrogels, which facilitated the entry of water molecules. The FTIR experiment was conducted, and the spectra are displayed in Fig. 1J. No new functional groups were generated in the GO@PEGDA/CMC and PP/GO@PEGDA/CMC hydrogels.

3.2. Metal ion release from the PP/GO@PEGDA/CMC hydrogels

Randomly selected fields of view were used for EDS analysis (Fig. 2A). According to the EDS mapping (Fig. 2B–F) and qualitative results (Fig. 2G), the peaks of five metal elements (iron, magnesium, copper, zinc, and manganese ions) appeared in the sample. This indicated that the metal ions in PP were successfully loaded onto GO. The concentration of various elements in PP decoction (1 g/mL) is shown in Table 1. ICP-MS was employed to prove that the release of metal ions was successful. The results showed that the metal elements were continuously released from the gel with time (Fig. 2H and I). The release rates and element contents were different. The iron and magnesium ions contents were higher than those of manganese, zinc, and copper ions. A certain promotion effect on bone regeneration was realized by the functional complementation of beneficial elements, which depended on the synergistic effects of various elements.

3.3. PP/GO@PEGDA/CMC induced macrophage M2-type differentiation in vitro

Macrophages are a unique subtype of immunocyte with two major phenotypes, M1 and M2. M1 macrophages lead to an inflammatory response and release IL-1β, TNF-α, and IL-6; M2 macrophages contribute to the osteogenic differentiation of osteoblasts and resolution of

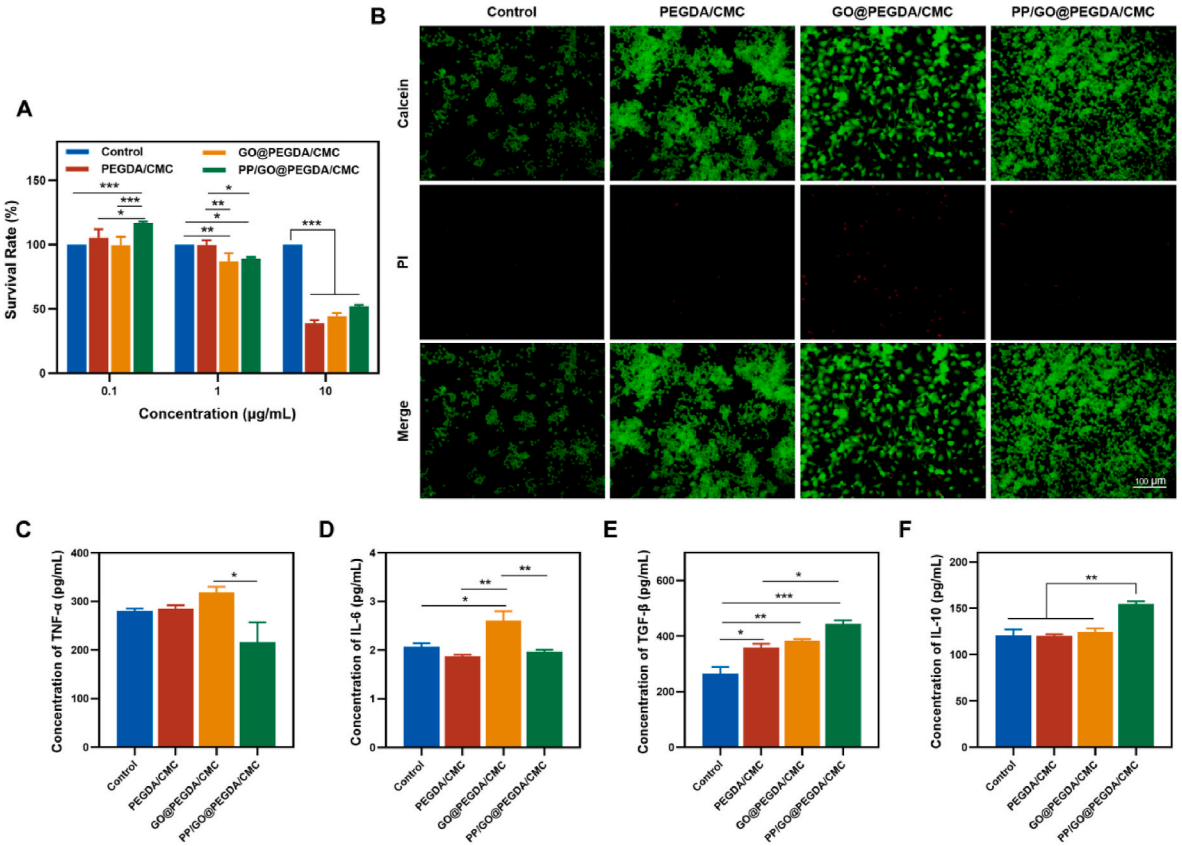

Fig. 3. Viability of Raw 264.7 macrophages and PP/GO@PEGDA/CMC hydrogel-conditioned media promoting the release of secretory factors from M2 macrophages. (A) CCK-8 assay of Raw 264.7 macrophages cultured in various conditioned media. (B) Fluorescence staining of Raw 264.7 macrophages cultured within various hydrogels over 48 h; the living cells were labeled with calcein-AM (green fluorescence), while the dead cells were labeled with PI (red fluorescence). (C) The secretion level of TNF-α (M1 marker) in the conditioned media. (D) The secretion level of IL-6 (M1 marker) in the conditioned media. (E) The secretion level of TGF-β (M2 marker) in the conditioned media. (F) The secretion level of IL-10 (M2 marker) in the conditioned media. *$p < 0.05$, **$p < 0.01$, and ***$p < 0.001$; mean ± SD; n = 6. (For interpretation of the references to colour in this figure legend, the reader is referred to the Web version of this article.)

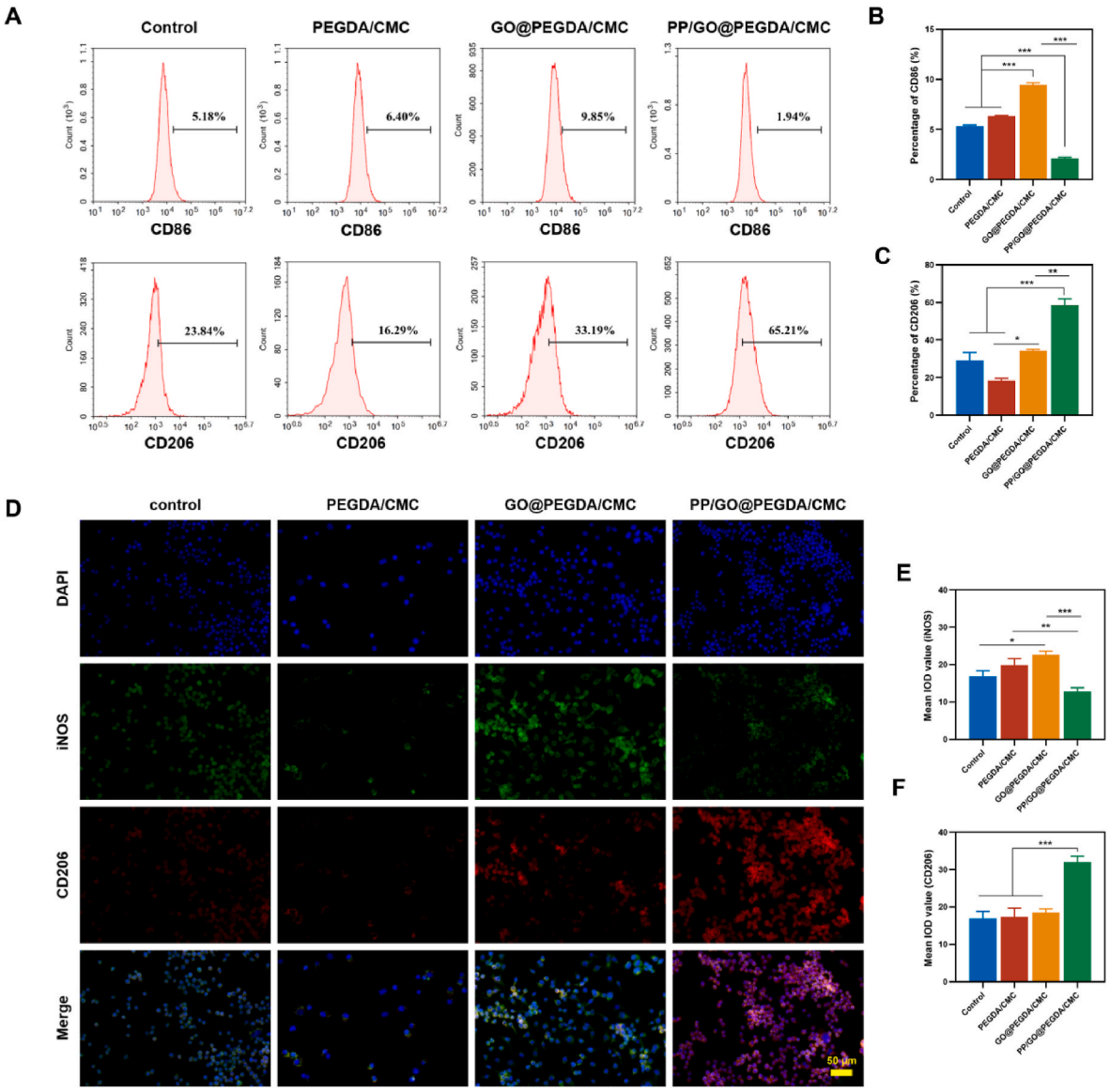

Fig. 4. PP/GO@PEGDA/CMC hydrogel-conditioned media promoting the M2 polarization of macrophages. (A) Proportions of CD86 (M1 marker) and CD206 (M2 marker) detected by FCM after 48 h of treatment. (B) Quantification of the proportion of CD86-positive macrophages (n = 3). (C) Quantification of the proportion of CD206-positive macrophages (n = 3). (D) Immunofluorescence staining following 48 h of culture in different conditioned media. The blue, green, and red colors represent DAPI, iNOS, and CD206 fluorescence, respectively. (E) Quantitative analysis of IOD for iNOS expression (n = 6). (F) Quantitative analysis of IOD for CD206 expression(n = 6). *$p < 0.05$, **$p < 0.01$, and ***$p < 0.001$; mean ± SD. (For interpretation of the references to colour in this figure legend, the reader is referred to the Web version of this article.)

inflammation by secreting IL-10, IL-4, and TGF-β. In the process of bone tissue repair, inflammation tends to result in delayed bone healing and fracture remodeling [46]. The inhibition of inflammation can promote bone formation in the bone defect area. The tissue microenvironment regulates the interconversion of M1 and M2 macrophages, which is important for tissue repair [47]. However, in many traditional design strategies, inert biomaterials have always been considered foreign bodies that result in a foreign body reaction along with excessive inflammation, thereby interfering with the speed and quality of osseointegration [48]. Therefore, an ideal biomaterial should be designed to modulate the local immune environment against pro-inflammatory responses and diminish host responses. With advancements in the field of osteoimmunology, bone regeneration and the immune system are closely linked in both physiological and pathological conditions.

In the early stage of inflammation, macrophages are activated and polarized to an M1 phenotype, which produces pro-inflammatory cytokines, such as IL-6 and TNF-α. At present, research on materials related to bone immune regulation and regeneration, especially bone induction materials rich in multiple metal ions, is scarce. In the present study, the PP/GO@PEGDA/CMC hydrogel could be modified to perform an "osteoimmunomodulatory" function. Macrophages are predominantly polarized to an M2 phenotype and produce cytokines, including IL-10, IL-4, and TGF-β, which contribute to tissue repair and the resolution of inflammation.

To verify whether hydrogels could immunomodulate new bone regeneration, PEGDA/CMC, GO@PEGDA/CMC, and PP/GO@PEGDA/CMC were fabricated. Raw 264.7 macrophages were successfully cultured and applied to the polarization experiments in vitro. Good biocompatibility is considered to be important for bone repair materials. Firstly, CCK-8 was used to detect the proliferation ability of the cells (Fig. 3A). The results showed that 0.1 and 1 μg/mL hydrogel-conditioned media were nontoxic, and the 1 μg/mL concentration was used for subsequent experiments (the GO concentration was 1 μg/mL in

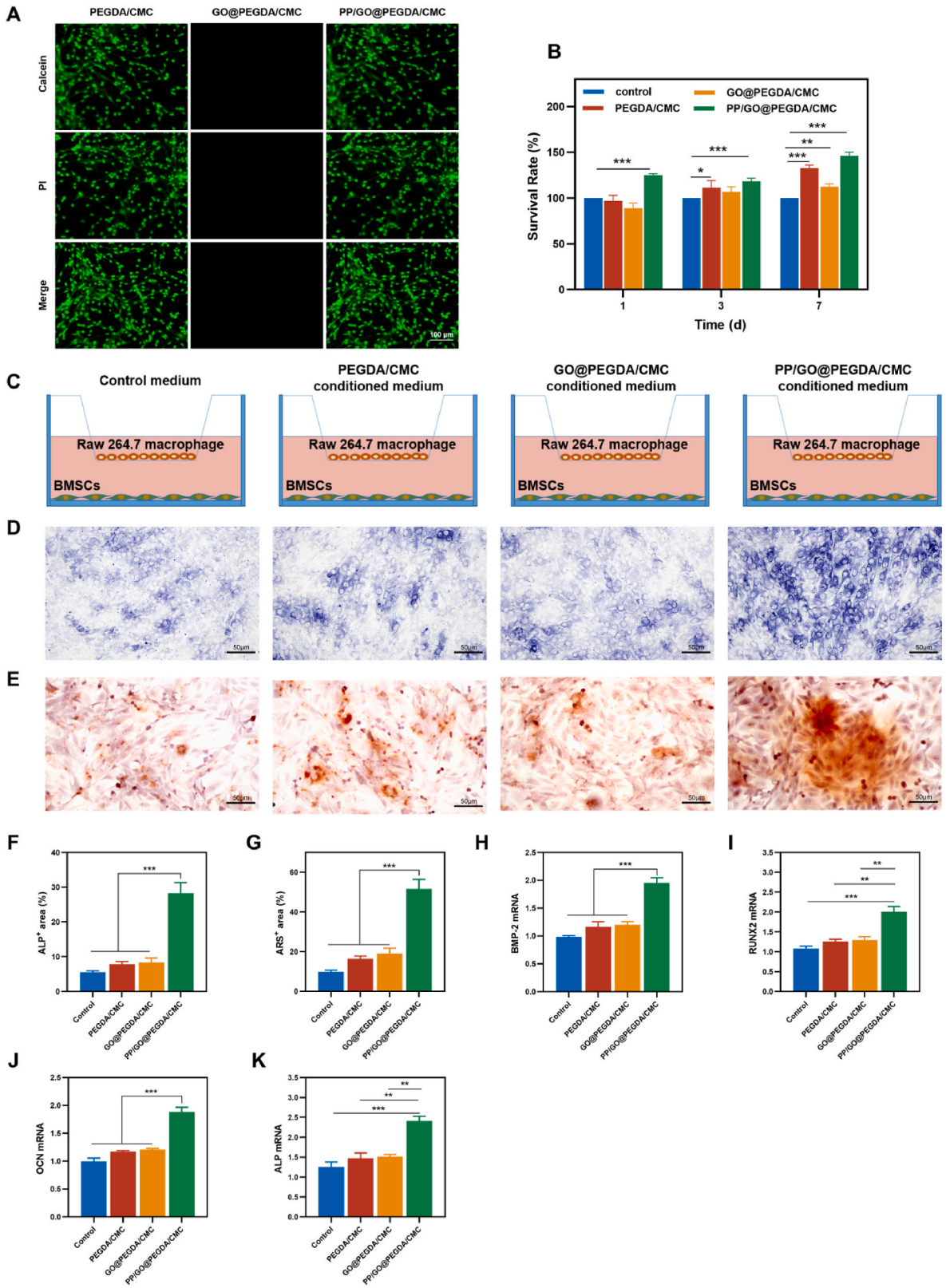

Fig. 5. PP/GO@PEGDA/CMC hydrogel-conditioned medium-treated Raw 264.7 macrophages promote the osteogenesis of BMSCs. (A) Live/dead cell staining of BMSCs cultured on various hydrogels at day 3. (B) CCK-8 assay of BMSCs cultured in various hydrogel-conditioned medium at days 1, 3, and 7 (n = 6). (C) Schematic diagram of the co-culture system. (D) ALP staining of BMSCs after 7 days of co-culture with different hydrogel-conditioned media-treated macrophages. (E) ARS staining of BMSCs after 14 days of co-culture with different hydrogel-conditioned media-treated macrophages. (F) The positive area in ALP staining (n = 3). (G) The positive area in ARS staining (n = 3). RT-qPCR analyses of (H) BMP-2, (I) Runx-2, (J) OCN, and (K) ALP mRNA expression in BMSCs after 7 days of co-culture with different hydrogel-conditioned media-treated macrophages (n = 3).*$p < 0.05$, **$p < 0.01$, and ***$p < 0.001$; mean ± SD.

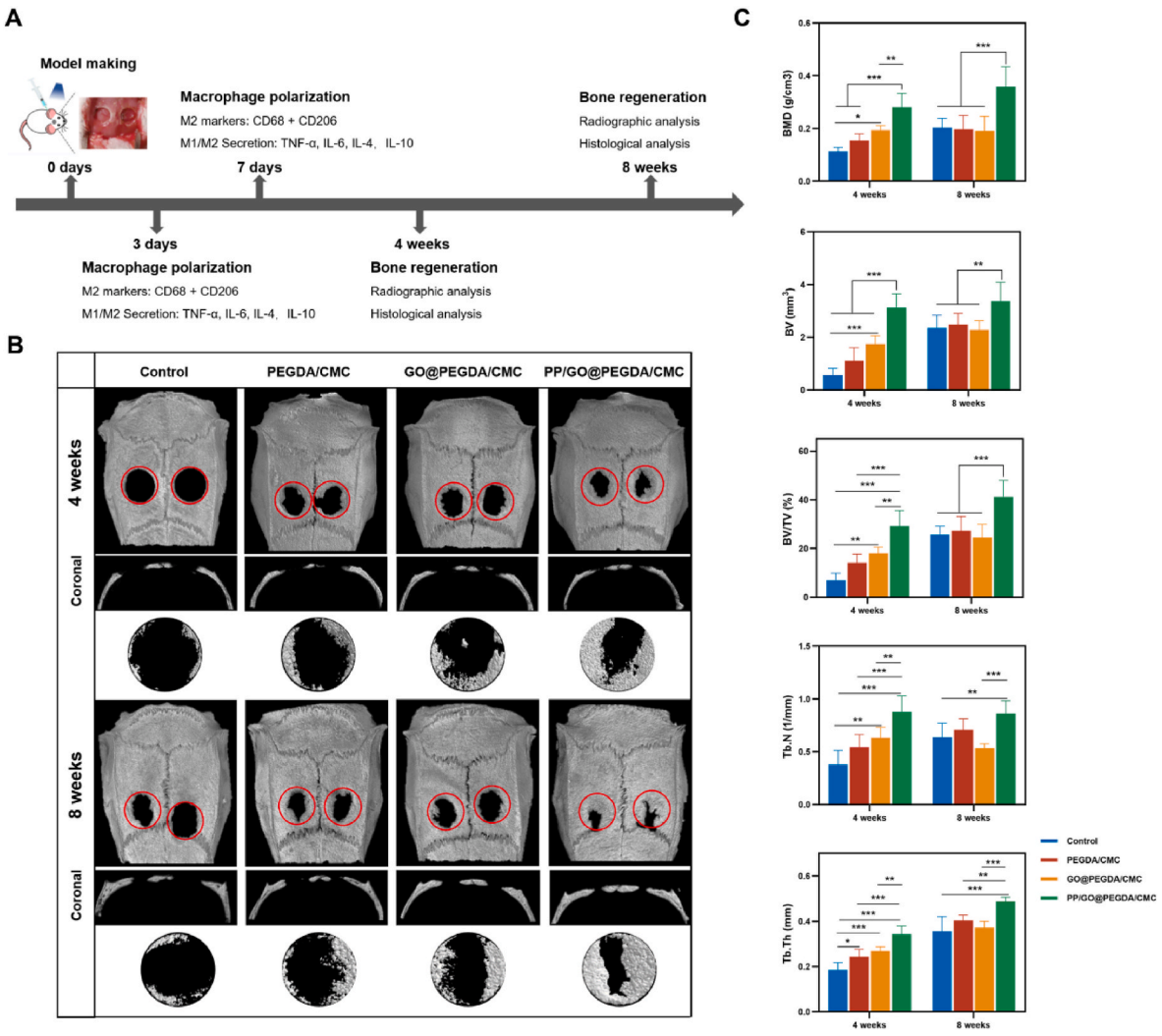

Fig. 6. Bone regeneration evaluation of PEGDA/CMC, GO@PEGDA/CMC, and PP/GO@PEGDA/CMC scaffolds at 4 and 8 weeks. (A) Schematic diagram of the steps followed in the in vivo experiments. (B) 3D reconstruction images showing the micro-CT analysis of the defect site (red circles) repaired by different scaffolds for 4 and 8 weeks post-implantation. Micro-CT 3D reconstruction images showing the best bone defect healing outcome in the PP/GO@PEGDA/CMC hydrogel group. (C) Quantification analysis of BMD, BV, BV/TV, Tb.N, and Tb.Th showing that the PP/GO@PEGDA/CMC group had the most new bone tissue. $*p < 0.05$, $**p < 0.01$, and $***p < 0.001$; mean ± SD; n = 6. (For interpretation of the references to colour in this figure legend, the reader is referred to the Web version of this article.)

the PP/GO@PEGDA/CMC hydrogel-conditioned medium, and the PP concentration was 0.175 μg/mL). The live/dead cell staining results (Fig. 3B) supported this viewpoint. To verify that the PP/GO@PEGDA/CMC hydrogels could induce macrophage M2-type differentiation, ELISA were performed (Fig. 3C–F). The results demonstrated that after stimulation with PP/GO@PEGDA/CMC for 48 h, the Raw 264.7 macrophages presented a trend toward the M2 phenotype.

FCM analysis (Fig. 4A) also revealed that CD206 (the marker of the M2 phenotype) was more highly expressed in the PP/GO@PEGDA/CMC group. Furthermore, the expression of CD86 (the marker of the M1 phenotype) decreased in Raw 264.7 macrophages after the PP/GO@PEGDA/CMC treatment (Fig. 4B and C). These results confirmed that the PEGDA/CMC material loaded with PP/GO successfully induced macrophage differentiation into the M2-type by releasing ions.

To further investigate the influence of the PP/GO@PEGDA/CMC hydrogel on macrophage differentiation, a cellular immunofluorescence assay was performed to examine the effect of hydrogel samples on Raw 264.7 macrophages (Fig. 4D). Pretreated Raw 264.7 macrophages were stimulated with different hydrogels for 48 h and significantly higher CD206 immunofluorescence positive staining was observed in the PP/GO@PEGDA/CMC group. The expression level of iNOS (the marker of the M1 phenotype) significantly decreased. Quantitative analysis of the experimental results was performed using Image-Pro Plus 6.0 (Fig. 4E and F). Briefly, the PP/GO@PEGDA/CMC hydrogel promoted the transformation of macrophages into the M2 type.

3.4. Osteogenic differentiation of BMSCs in a co-culture system

Live/dead cell staining indicated that BMSCs could grow on the hydrogels (Fig. 5A). CCK-8 results indicated that various hydrogel-conditioned media had no cytotoxicity on days 1, 3, or 7 (Fig. 5B). ALP and ARS staining indicated that macrophages treated with PP/GO@PEGDA/CMC hydrogel-conditioned medium were greatly beneficial for BMSCs osteogenesis (Fig. 5D–G). The transcription levels of osteogenesis-related genes were prominently increased by the activation of macrophages treated with PP/GO@PEGDA/CMC hydrogel-conditioned medium (Fig. 5H–K).

3.5. Radiographic analysis of bone regeneration

The time axis of the in vivo experiments is shown in Fig. 6A. Micro-CT was conducted to evaluate the extent of new bone formation in the

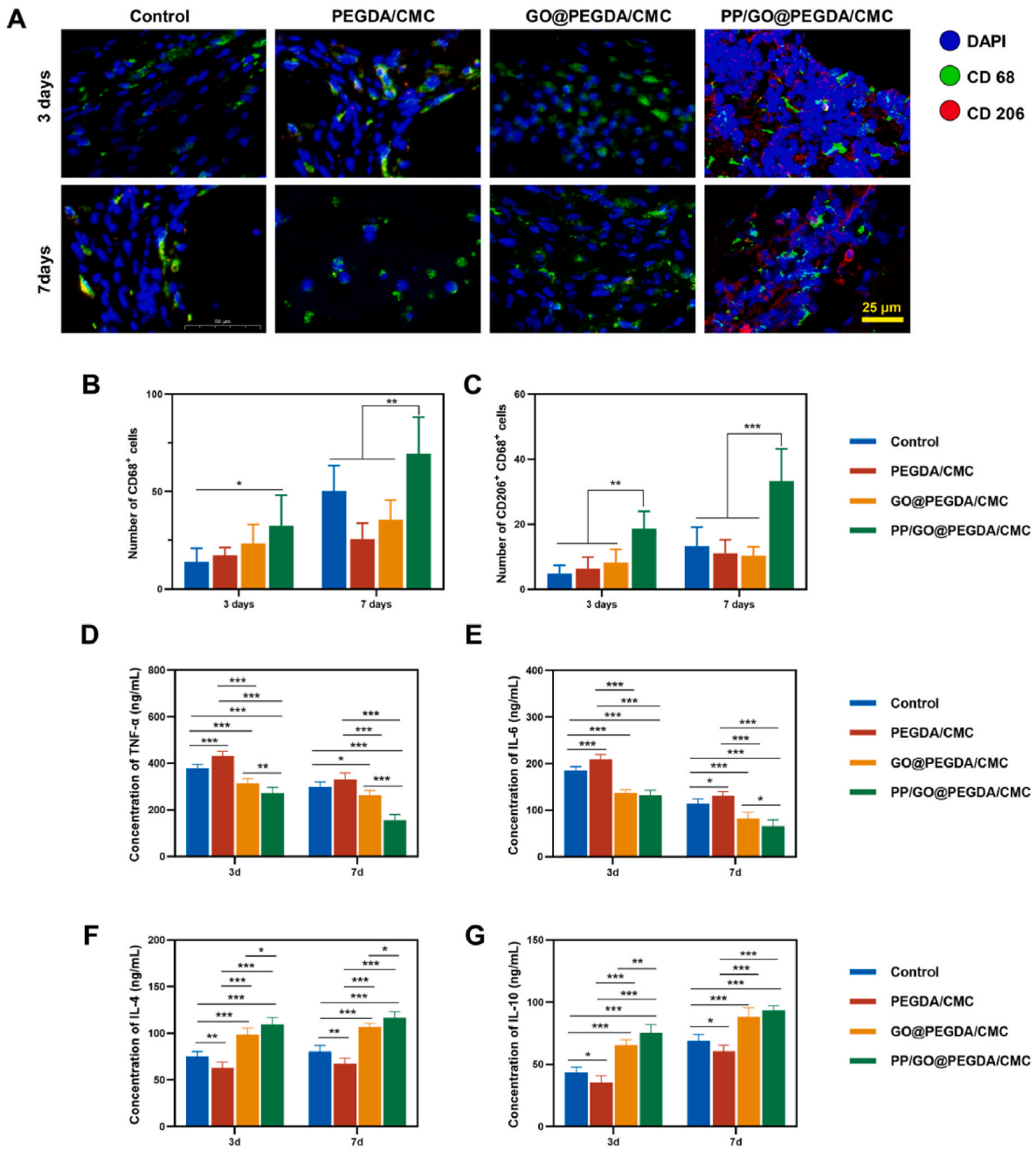

Fig. 7. PP/GO@PEGDA/CMC hydrogels promoting the M2 polarization of macrophages in vivo. (A) Immunofluorescence evaluation of macrophage polarization at the implant site for PBS, PEGDA/CMC, GO@PEGDA/CMC, and PP/GO@PEGDA/CMC at 3 and 7 days. Blue, green, and red colors represent DAPI, CD68, and CD206 fluorescence, respectively. (B) Image analysis of $CD68^+$ cells in the bone defect area. (C) Image analysis of $CD68^+$, $CD206^+$ (M2 macrophages) in the area of the bone defects after the PEGDA/CMC, GO@PEGDA/CMC, and PP/GO@PEGDA/CMC implantation. (D) Expression level of TNF-α (M1 marker) in rat plasma after induction using scaffolds for 3 and 7 days. (E) Expression level of IL-6 (M1 marker) in rat plasma after induction using scaffolds for 3 and 7 days. (F) Expression level of IL-4 (M2 marker) in rat plasma after induction using scaffolds for 3 and 7 days. (G) Expression level of IL-10 (M2 marker) in rat plasma after induction using scaffolds for 3 and 7 days. $^*p < 0.05$, $^{**}p < 0.01$, and $^{***}p < 0.001$; mean ± SD; n = 6. (For interpretation of the references to colour in this figure legend, the reader is referred to the Web version of this article.)

bone defects at 4 and 8 weeks. As shown in Fig. 6B, the 3D reconstruction of the skull indicated that the PP/GO@PEGDA/CMC group exhibited an excellent bone regeneration capacity compared with the other groups; the sagittal plane of the bone defect also confirmed this viewpoint. The quantification analysis of BV and BV/TV of the newly formed bone showed that the BV and BV/TV of the PP/GO@PEGDA/CMC group were remarkably higher than those of the other groups at both 4 and 8 weeks (Fig. 6C). Quantification of the BMD, Tb.N, and Tb.Th showed that PP/GO@PEGDA/CMC achieved superior bone defect repair efficacy, which was consistent with the BV and BV/TV results (Fig. 6C). The extent of bone regeneration was in the following order: PP/GO@PEGDA/CMC > GO@PEGDA/CMC > PEGDA/CMC > control. Interestingly, it was found that the osteogenesis speed at 4 weeks was better than that at 8 weeks in the PP/GO@PEGDA/CMC group.

3.6. Effects of PP/GO@PEGDA/CMC on macrophage activation in vivo

After 3 and 7 days of the hydrogel implantation, the samples were

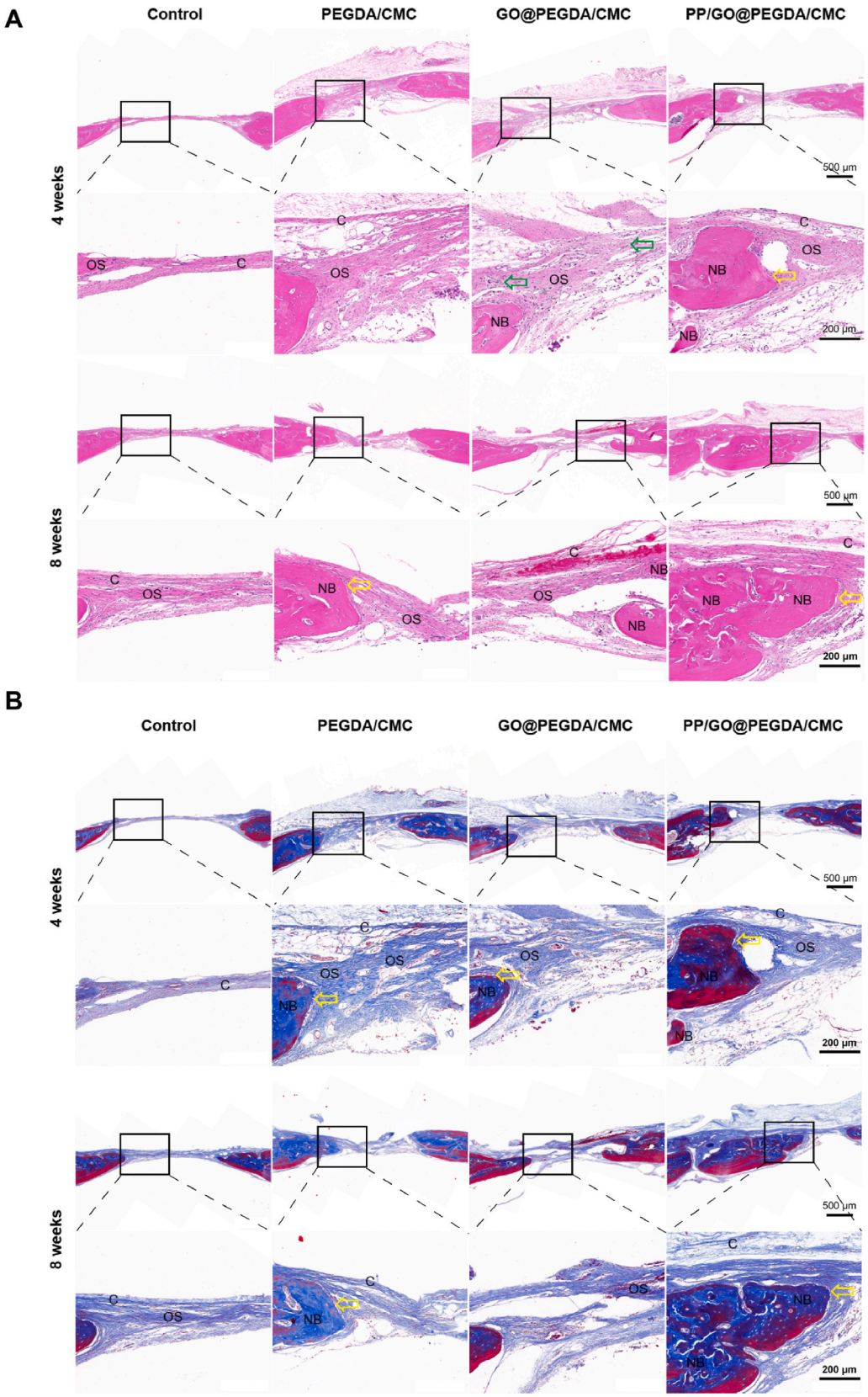

Fig. 8. Histological evaluation of bone regeneration after implantation. (A) HE staining of the calvarial defects at 4 and 8 weeks post-implantation. (B) Masson's staining of specimens of bone defect repair at 4 and 8 weeks post-implantation. The regions highlighted by the black box are shown in the high-magnification images below. NB, new bone; OS, osteoid tissue; C, connective tissue. Yellow arrows indicate osteoblasts and green arrows indicate undegraded gel scaffold. (For interpretation of the references to colour in this figure legend, the reader is referred to the Web version of this article.)

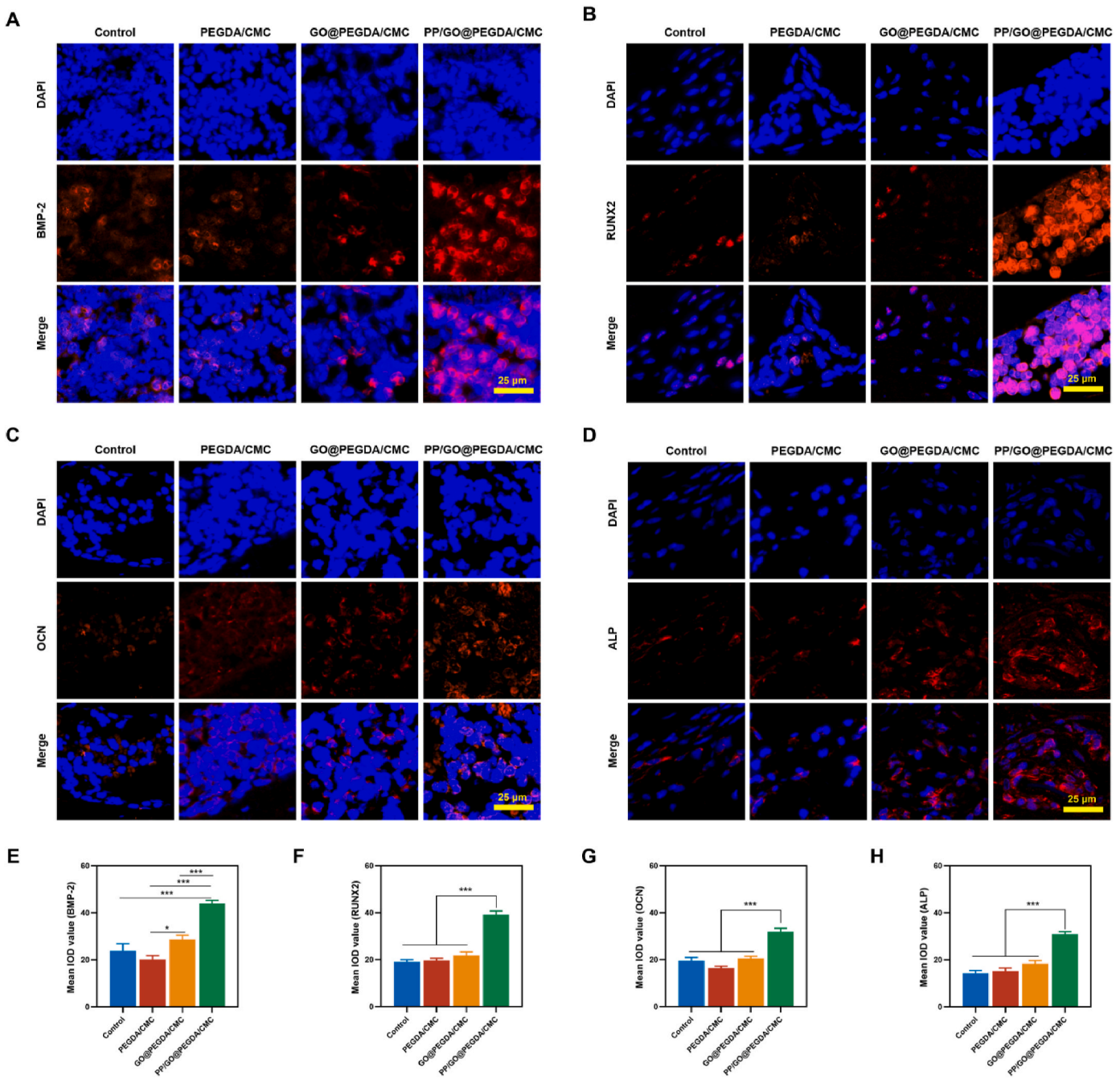

Fig. 9. Immunofluorescence analysis of tissue repair factors at 8 weeks in the area of bone defects. (A) Immunofluorescence analysis of BMP-2 expression. (B) Immunofluorescence analysis of RUNX2 expression. (C) Immunofluorescence analysis of OCN expression. (D) Immunofluorescence analysis of ALP expression. (E) Quantitative analysis of IOD for BMP-2 expression. (F) Quantitative analysis of IOD for RUNX2 expression. (G) Quantitative analysis of IOD for OCN expression. (H) Quantitative analysis of IOD for ALP expression. $*p < 0.05$, $**p < 0.01$, and $***p < 0.001$; mean ± SD; n = 6.

prepared to assess the activation and function of the macrophages. As shown in Fig. 7A, the total macrophage levels were remarkably elevated in the PP/GO@PEGDA/CMC group compared to in the other groups. The expression level of macrophages on day 7 was higher than that on day 3 in all groups. As expected, the population of M2 macrophages ($CD68^+$, $CD206^+$) was greater than that of the other three groups following PP/GO@PEGDA/CMC implantation at day 3. In contrast, the M2 macrophage ($CD68^+$, $CD206^+$) levels decreased in the GO@PEGDA/CMC group on day 7 compared to those in the control and PEGDA/CMC groups. This suggests that PP/GO@PEGDA/CMC with sustained release of metal ions could activate macrophages polarization, thereby stimulating the M2 phenotype in the early stage. Quantitative analysis of the number of macrophages showed that M0 ($CD68^+$) and M2 macrophage ($CD68^+$, $CD206^+$) levels were higher in the PP/GO@PEGDA/CMC group than in the other three groups (Fig. 7B and C).

To further assess the effects of hydrogels on macrophage activation, inflammation-related indicators in plasma were analyzed using ELISA kits (Fig. 7D–G). The results indicated that the PP/GO@PEGDA/CMC hydrogels promoted the M2-type differentiation of macrophages by secreting high levels of IL-10 and IL-4. They also decreased the M1-type differentiation of macrophages by secreting low levels of TNF-α and IL-6. With the increase in IL-10 and IL-4 levels, BMP-2 was recruited to secrete osteoblast-related proteins to promote the differentiation of mesenchymal stem cells (MSCs) into osteoblasts. This indicated that M1 and

M2 were in dynamic equilibrium. It was speculated that the PP/GO@PEGDA/CMC hydrogels could optimize the ratio of M1 to M2 to improve the immune microenvironment.

3.7. Histological analyses

HE staining and Masson's staining were used to reveal new bone formation in all groups at 4 and 8 weeks. As shown in Fig. 8A, the bone defect was filled and depressed by connective tissue, with fewer osteoblasts in the control group. In the PEGDA/CMC and GO@PEGDA/CMC groups, there was a certain degree of increase in both the osteoid tissue and new bone. In the PP/GO@PEGDA/CMC group, the bone defects were filled with a large amount of osteoid tissue and freshly formed woven bone at 4 weeks, and the bone defects seemed to almost complete bone regeneration with mature bone matrix and bone trabecular at 8 weeks. Masson's trichrome staining corroborated these results. As shown in Fig. 8B, the PP/GO@PEGDA/CMC hydrogel treatment promoted the formation of mature lamellar bone (dark red staining) at 8 weeks. The HE and Masson staining of bone tissue also confirmed that the new bone formation ability of PP/GO@PEGDA/CMC was much greater than that of the other groups. BMP-2 is vital for cartilage formation and development. The results indicated that the PP/GO@PEGDA/CMC hydrogels displayed high expression of BMP-2 compared with other groups at 8 weeks (Fig. 9A). RUNX-2, OCN, and ALP are usually used to evaluate the degree of bone formation. The immunofluorescence analysis of the skull defect areas of osteogenic markers (RUNX-2, OCN, and ALP) showed that the osteogenic activity of the PP/GO@PEGDA/CMC group was higher than that of the other three groups at 8 weeks (Fig. 9B–D). In addition, the expression of BMP-2, RUNX2, OCN, and ALP in the defect areas was higher than that of the other three groups in the metaphase of bone repair (Fig. S2). OPN-positive cells were observed within the defect areas in the PP/GO@PEGDA/CMC group, and the expression of OPN was higher than that in the other three groups at 4 and 8 weeks (Fig. S3 and Fig. S4).

4. Conclusion

In this study, a new mineral-organic nano-compound hydrogel (PP/GO@PEGDA/CMC) was generated and characterized. PP provided abundant metal ions, and GO provided sufficient mechanical strength to the PEGDA/CMC molecular network to overcome the support obstacle. Experiments confirmed that metal ions were loaded and released from the PP/GO@PEGDA/CMC hydrogel in a controlled manner to promote M2 polarization, which is related to bone remodeling. It was further revealed that the PP/GO@PEGDA/CMC hydrogel mediated the early immune response to induce the generation of TGF-β, IL-10, and IL-4 to promote the secretion of BMP-2 from BMSCs. The critical-sized rat calvarial defect model was utilized, and the levels of ALP, RUNX2, OCN, and OPN were markedly increased in the defects after the implantation of the PP/GO@PEGDA/CMC hydrogels. Noticeable bone reconstruction was performed. This study highlights a biomaterial that modulates the immune microenvironment and achieves greater bone repair efficacy. This suggests considerable potential for the field of biomaterials and medicine.

Credit author statement

Changcan Shi and Yinting Yu conducted the experiments, analyzed the data, produced the figures, and wrote the manuscript. Hao Zhai and Chenxu Wei contributed to rheological and mechanical testing. Huanjin Liu and Dan Wang contributed to the animal experiments. Mengyu Guo and Wenxin Wang assisted with editing the manuscript. Hongjuan Wu, Zhipeng Chen, and Guojun Yan helped review and check the manuscript. Weidong Li and Ting Cai put forward ideas and designed the experiments. Weidong Li provided funding.

Declaration of competing interest

The authors declare that they have no known competing financial interests or personal relationships that could have appeared to influence the work reported in this paper.

Data availability

Data will be made available on request.

Acknowledgements

The authors acknowledge funding support from the National Science Foundation of China (Grant No. 81373970, No. 81773902 and No. 81973484).

Appendix A. Supplementary data

Supplementary data to this article can be found online at https://doi.org/10.1016/j.mtbio.2023.100753.

References

[1] A.-M. Wu, C. Bisignano, S.L. James, G.G. Abady, A. Abedi, E. Abu-Gharbieh, R. K. Alhassan, V. Alipour, J. Arabloo, M. Asaad, W.N. Asmare, A.F. Awedew, M. Banach, S.K. Banerjee, A. Bijani, T.T.M. Birhanu, S.R. Bolla, L.A. Cámera, J.-C. Chang, D.Y. Cho, M.T. Chung, R.A.S. Couto, X. Dai, L. Dandona, R. Dandona, F. Farzadfar, I. Filip, F. Fischer, A.A. Fomenkov, T.K. Gill, B. Gupta, J.A. Haagsma, A. Haj-Mirzaian, S. Hamidi, S.I. Hay, I.M. Ilic, M.D. Ilic, R.Q. Ivers, M. Jürisson, R. Kalhor, T. Kanchan, T. Kavetskyy, R. Khalilov, E.A. Khan, M. Khan, C.J. Kneib, V. Krishnamoorthy, G.A. Kumar, N. Kumar, R. Lalloo, S. Lasrado, S.S. Lim, Z. Liu, A. Manafi, N. Manafi, R.G. Menezes, T.J. Meretoja, B. Miazgowski, T.R. Miller, Y. Mohammad, A. Mohammadian-Hafshejani, A.H. Mokdad, C.J.L. Murray, M. Naderi, M.D. Naimzada, V.C. Nayak, C.T. Nguyen, R. Nikbakhsh, A.T. Olagunju, N. Otstavnov, S.S. Otstavnov, J.R. Padubidri, J. Pereira, H.Q. Pham, M. Pinheiro, S. Polinder, H. Pourchamani, N. Rabiee, A. Radfar, M.H.U. Rahman, D.L. Rawaf, S. Rawaf, M.R. Saeb, A.M. Samy, L. Sanchez Riera, D.C. Schwebel, S. Shahabi, M. A. Shaikh, A. Soheili, R. Tabarés-Seisdedos, M.R. Tovani-Palone, B.X. Tran, R. S. Travillian, P.R. Valdez, T.J. Vasankari, D.Z. Velazquez, N. Venketasubramanian, G.T. Vu, Z.-J. Zhang, T. Vos, Global, regional, and national burden of bone fractures in 204 countries and territories, 1990–2019: a systematic analysis from the Global Burden of Disease Study 2019, The Lancet Healthy Longevity 2 (2021) e580–e592, https://doi.org/10.1016/S2666-7568(21)00172-0.

[2] A. Salhotra, H.N. Shah, B. Levi, M.T. Longaker, Mechanisms of bone development and repair, Nat. Rev. Mol. Cell Biol. 21 (2020) 696–711, https://doi.org/10.1038/s41580-020-00279-w.

[3] S. Stamnitz, A. Klimczak, Mesenchymal stem cells, bioactive factors, and scaffolds in bone repair: from research perspectives to clinical practice, Cells 10 (2021) 1925, https://doi.org/10.3390/cells10081925.

[4] L. Davenport Huyer, S. Pascual-Gil, Y. Wang, S. Mandla, B. Yee, M. Radisic, Advanced strategies for modulation of the material–macrophage interface, Adv. Funct. Mater. 30 (2020), 1909331, https://doi.org/10.1002/adfm.201909331.

[5] A. Vishwakarma, N.S. Bhise, M.B. Evangelista, J. Rouwkema, M.R. Dokmeci, A. M. Ghaemmaghami, N.E. Vrana, A. Khademhosseini, Engineering immunomodulatory biomaterials to tune the inflammatory response, Trends Biotechnol. 34 (2016) 470–482, https://doi.org/10.1016/j.tibtech.2016.03.009.

[6] S. Franz, S. Rammelt, D. Scharnweber, J.C. Simon, Immune responses to implants - a review of the implications for the design of immunomodulatory biomaterials, Biomaterials 32 (2011) 6692–6709, https://doi.org/10.1016/j.biomaterials.2011.05.078.

[7] D.P. Vasconcelos, A.P. Águas, M.A. Barbosa, P. Pelegrín, J.N. Barbosa, The inflammasome in host response to biomaterials: bridging inflammation and tissue regeneration, Acta Biomater. 83 (2019) 1–12, https://doi.org/10.1016/j.actbio.2018.09.056.

[8] J. Li, F. Han, J. Ma, H. Wang, J. Pan, G. Yang, H. Zhao, J. Zhao, J. Liu, Z. Liu, B. Li, Targeting endogenous hydrogen peroxide at bone defects promotes bone repair, Adv. Funct. Mater. 32 (2022), 2111208, https://doi.org/10.1002/adfm.202111208.

[9] X. Xue, Y. Hu, Y. Deng, J. Su, Recent advances in design of functional biocompatible hydrogels for bone tissue engineering, Adv. Funct. Mater. 31 (2021), 2009432, https://doi.org/10.1002/adfm.202009432.

[10] B.O. Okesola, S. Ni, B. Derkus, C.C. Galeano, A. Hasan, Y. Wu, J. Ramis, L. Buttery, J.I. Dawson, M. D'Este, R.O.C. Oreffo, D. Eglin, H. Sun, A. Mata, Growth-factor free multicomponent nanocomposite hydrogels that stimulate bone formation, Adv. Funct. Mater. 30 (2020), 1906205, https://doi.org/10.1002/adfm.201906205.

[11] J. Li, D.J. Mooney, Designing hydrogels for controlled drug delivery, Nat. Rev. Mater. 1 (2016), 16071, https://doi.org/10.1038/natrevmats.2016.71.

[12] N. Annabi, A. Tamayol, J.A. Uquillas, M. Akbari, L.E. Bertassoni, C. Cha, G. Camci-Unal, M.R. Dokmeci, N.A. Peppas, A. Khademhosseini, 25th anniversary article:

rational design and applications of hydrogels in regenerative medicine, Adv. Mater. 26 (2014) 85–124, https://doi.org/10.1002/adma.201303233.
[13] Y. Li, J. Rodrigues, H. Tomás, Injectable and biodegradable hydrogels: gelation, biodegradation and biomedical applications, Chem. Soc. Rev. 41 (2012) 2193–2221, https://doi.org/10.1039/C1CS15203C.
[14] Z.-K. Cui, S. Kim, J.J. Baljon, B.M. Wu, T. Aghaloo, M. Lee, Microporous methacrylated glycol chitosan-montmorillonite nanocomposite hydrogel for bone tissue engineering, Nat. Commun. 10 (2019) 3523, https://doi.org/10.1038/s41467-019-11511-3.
[15] C.-S. Lee, H.S. Hwang, S. Kim, J. Fan, T. Aghaloo, M. Lee, Inspired by nature: facile design of nanoclay–organic hydrogel bone sealant with multifunctional properties for robust bone regeneration, Adv. Funct. Mater. 30 (2020), 2003717.
[16] S. Bai, X. Zhang, X. Lv, M. Zhang, X. Huang, Y. Shi, C. Lu, J. Song, H. Yang, Bioinspired mineral–organic bone adhesives for stable fracture fixation and accelerated bone regeneration, Adv. Funct. Mater. 30 (2020), 1908381, https://doi.org/10.1002/adfm.201908381.
[17] W. Wang, K.W.K. Yeung, Bone grafts and biomaterials substitutes for bone defect repair: a review, Bioact. Mater. 2 (2017) 224–247, https://doi.org/10.1016/j.bioactmat.2017.05.007.
[18] M.P. Nikolova, M.S. Chavali, Recent advances in biomaterials for 3D scaffolds: a review, Bioact. Mater. 4 (2019) 271–292, https://doi.org/10.1016/j.bioactmat.2019.10.005.
[19] V.M. Schatkoski, T. Larissa do Amaral Montanheiro, B.R. Canuto de Menezes, R. M. Pereira, K.F. Rodrigues, R.G. Ribas, D. Morais da Silva, G.P. Thim, Current advances concerning the most cited metal ions doped bioceramics and silicate-based bioactive glasses for bone tissue engineering, Ceram. Int. 47 (2021) 2999–3012, https://doi.org/10.1016/j.ceramint.2020.09.213.
[20] Z. Chen, W. Zhang, M. Wang, L.J. Backman, J. Chen, Effects of zinc, magnesium, and iron ions on bone tissue engineering, ACS Biomater. Sci. Eng. 8 (2022) 2321–2335, https://doi.org/10.1021/acsbiomaterials.2c00368.
[21] D. Hernández-Escobar, S. Champagne, H. Yilmazer, B. Dikici, C.J. Boehlert, H. Hermawan, Current status and perspectives of zinc-based absorbable alloys for biomedical applications, Acta Biomater. 97 (2019) 1–22, https://doi.org/10.1016/j.actbio.2019.07.034.
[22] C. Wu, W. Fan, Y. Zhu, M. Gelinsky, J. Chang, G. Cuniberti, V. Albrecht, T. Friis, Y. Xiao, Multifunctional magnetic mesoporous bioactive glass scaffolds with a hierarchical pore structure, Acta Biomater. 7 (2011) 3563–3572, https://doi.org/10.1016/j.actbio.2011.06.028.
[23] J. Vormann, Magnesium: nutrition and metabolism, Mol. Aspect. Med. 24 (2003) 27–37, https://doi.org/10.1016/s0098-2997(02)00089-4.
[24] X. Shen, Y. Zhang, P. Ma, L. Sutrisno, Z. Luo, Y. Hu, Y. Yu, B. Tao, C. Li, K. Cai, Fabrication of magnesium/zinc-metal organic framework on titanium implants to inhibit bacterial infection and promote bone regeneration, Biomaterials 212 (2019) 1–16, https://doi.org/10.1016/j.biomaterials.2019.05.008.
[25] D. Zhao, F. Witte, F. Lu, J. Wang, J. Li, L. Qin, Current status on clinical applications of magnesium-based orthopaedic implants: a review from clinical translational perspective, Biomaterials 112 (2017) 287–302, https://doi.org/10.1016/j.biomaterials.2016.10.017.
[26] S. Yoshizawa, A. Chaya, K. Verdelis, E.A. Bilodeau, C. Sfeir, An in vivo model to assess magnesium alloys and their biological effect on human bone marrow stromal cells, Acta Biomater. 28 (2015) 234–239, https://doi.org/10.1016/j.actbio.2015.08.037.
[27] M. Yamaguchi, Role of zinc in bone formation and bone resorption, J. Trace Elem. Exp. Med. 11 (1998) 119–135, https://doi.org/10.1002/(SICI)1520–670X(1998)11:2/3<119::AID-JTRA5>3.0.CO;2-3.
[28] L. Rink, Zinc and the immune system, Proc. Nutr. Soc. 59 (2000) 541–552, https://doi.org/10.1017/S0029665100000781.
[29] D. Zhu, Y. Su, M.L. Young, J. Ma, Y. Zheng, L. Tang, Biological responses and mechanisms of human bone marrow mesenchymal stem cells to Zn and Mg biomaterials, ACS Appl. Mater. Interfaces 9 (2017) 27453–27461, https://doi.org/10.1021/acsami.7b06654.
[30] Q. Xu, R. Bauer, B.M. Hendry, T.-P. Fan, Z. Zhao, P. Duez, M.S. Simmonds, C. M. Witt, A. Lu, N. Robinson, D. Guo, P.J. Hylands, The quest for modernisation of traditional Chinese medicine, BMC Compl. Alternative Med. 13 (2013) 132, https://doi.org/10.1186/1472-6882-13-132.
[31] L. Liu, G.H. Zhao, Q.Q. Gao, Y.J. Chen, Z.P. Chen, Z.S. Xu, W.D. Li, Changes of mineralogical characteristics and osteoblast activities of raw and processed pyrites, RSC Adv. 7 (2017) 28373–28382, https://doi.org/10.1039/C7RA03970K.
[32] X. Zhu, Q. Gao, G. Zhao, H. Wang, L. Liu, Z. Chen, Y. Chen, L. Wu, Z. Xu, W. Li, Comparison study of bone defect healing effect of raw and processed pyritum in rats, Biol. Trace Elem. Res. 184 (2018) 136–147, https://doi.org/10.1007/s12011-017-1166-0.
[33] D. Wang, J. Hou, C. Xia, C. Wei, Y. Zhu, W. Qian, S. Qi, Y. Wu, Y. Shi, K. Qin, L. Wu, F. Yin, Z. Chen, W. Li, Multi-element processed pyritum mixed to β-tricalcium phosphate to obtain a 3D-printed porous scaffold: an option for treatment of bone defects, Mater Sci Eng C Mater Biol Appl 128 (2021), 112326, https://doi.org/10.1016/j.msec.2021.112326.
[34] H. Safiaghdam, H. Nokhbatolfoghahaei, A. Khojasteh, Therapeutic metallic ions in bone tissue engineering: a systematic review of the literature, Iran. J. Pharm. Res. (IJPR) 18 (2019) 101–118, https://doi.org/10.22037/ijpr.2020.112641.13894.
[35] K. Glenske, P. Donkiewicz, A. Köwitsch, N. Milosevic-Oljaca, P. Rider, S. Rofall, J. Franke, O. Jung, R. Smeets, R. Schnettler, S. Wenisch, M. Barbeck, Applications of metals for bone regeneration, Int. J. Mol. Sci. 19 (2018) 826, https://doi.org/10.3390/ijms19030826.
[36] X. Zhu, Q. Gao, G. Zhao, H. Wang, L. Liu, Z. Chen, Y. Chen, L. Wu, Z. Xu, W. Li, Comparison study of bone defect healing effect of raw and processed pyritum in rats, Biol. Trace Elem. Res. 184 (1) (2018) 136–147, https://doi.org/10.1016/j.jconrel.2022.12.031.
[37] L. Xu, S. Xu, T.Y. Xiang, L.W. Chen, W.X. Zhong, L. Zhu, H. Liu, L. Wu, W.D. Li, Y. T. Wang, B.C. Cai, J.H. Yao, R. Chen, W.F. Xin, G. Cao, Z.P. Chen, A novel peptide hydrogel of metal ion clusters for accelerating bone defect regeneration, J. Contr. Release 353 (2023) 738–751, https://doi.org/10.1007/s12011-017-1166-0.
[38] M. Christian, R. Mazzaro, V. Morandi, Bioinspired design of graphene-based materials, Adv. Funct. Mater. 30 (2020), 2007458, https://doi.org/10.1002/adfm.202007458.
[39] L. Chaabane, E. Beyou, A. El Ghali, M.H.V. Baouab, Comparative studies on the adsorption of metal ions from aqueous solutions using various functionalized graphene oxide sheets as supported adsorbents, J. Hazard Mater. 389 (2020), 121839, https://doi.org/10.1016/j.jhazmat.2019.121839.
[40] J. Ruan, X. Wang, Z. Yu, Z. Wang, Q. Xie, D. Zhang, Y. Huang, H. Zhou, X. Bi, C. Xiao, P. Gu, X. Fan, Enhanced physiochemical and mechanical performance of chitosan-grafted graphene oxide for superior osteoinductivity, Adv. Funct. Mater. 26 (2016) 1085–1097, https://doi.org/10.1002/adfm.201504141.
[41] Z. Li, S. Xiang, Z. Lin, E.N. Li, H. Yagi, G. Cao, L. Yocum, L. Li, T. Hao, K.K. Bruce, M.R. Fritch, H. Hu, B. Wang, P.G. Alexander, K.A. Khor, R.S. Tuan, H. Lin, Graphene oxide-functionalized nanocomposites promote osteogenesis of human mesenchymal stem cells via enhancement of BMP-SMAD1/5 signaling pathway, Biomaterials 277 (2021), 121082, https://doi.org/10.1016/j.biomaterials.2021.121082.
[42] L. Newman, D.A. Jasim, E. Prestat, N. Lozano, I. de Lazaro, Y. Nam, B.M. Assas, J. Pennock, S.J. Haigh, C. Bussy, K. Kostarelos, Splenic capture and *in vivo* intracellular biodegradation of biological-grade graphene oxide sheets, ACS Nano 14 (2020) 10168–10186, https://doi.org/10.1021/acsnano.0c03438.
[43] S.P. Mukherjee, A.R. Gliga, B. Lazzaretto, B. Brandner, M. Fielden, C. Vogt, L. Newman, A.F. Rodrigues, W. Shao, P.M. Fournier, M.S. Toprak, A. Star, K. Kostarelos, K. Bhattacharya, B. Fadeel, Graphene oxide is degraded by neutrophils and the degradation products are non-genotoxic, Nanoscale 10 (2018) 1180–1188, https://doi.org/10.1039/C7NR03552G.
[44] W. Wang, Y. Cao, X. Hu, S. Zhou, D. Zhu, D. Qi, S. Deng, Granular reduced graphene oxide/Fe3O4 hydrogel for efficient adsorption and catalytic oxidation of p-perfluorous nonenoxybenzene sulfonate, J. Hazard Mater. 386 (2020), 121662, https://doi.org/10.1016/j.jhazmat.2019.121662.
[45] Y. Zheng, B. Cheng, W. You, J. Yu, W. Ho, 3D hierarchical graphene oxide-NiFe LDH composite with enhanced adsorption affinity to Congo red, methyl orange and Cr(VI) ions, J. Hazard Mater. 369 (2019) 214–225, https://doi.org/10.1016/j.jhazmat.2019.02.013.
[46] S. Behzadi, G.A. Luther, M.B. Harris, O.C. Farokhzad, M. Mahmoudi, Nanomedicine for safe healing of bone trauma: opportunities and challenges, Biomaterials 146 (2017) 168–182, https://doi.org/10.1016/j.biomaterials.2017.09.005.
[47] T.A. Wynn, A. Chawla, J.W. Pollard, Macrophage biology in development, homeostasis and disease, Nature 496 (2013) 445–455, https://doi.org/10.1038/nature12034.
[48] J.M. Anderson, A. Rodriguez, D.T. Chang, Foreign body reaction to biomaterials, Semin. Immunol. 20 (2008) 86–100, https://doi.org/10.1016/j.smim.2007.11.004.

Abbreviations

PEGDA: poly(ethylene glycol) diacrylate
CMC: carboxymethyl chitosan
GO: graphene oxide
PP: processed pyritum
Photoinitiator 2959: 2-hydroxy-4-(2-hydroxyethoxy)-2-methylpropiophenone
IL: interleukin
TGF-β: transforming growth factor-β
TNF-α: tumor necrosis factor-α
OCN: osteocalcin
ALP: alkaline phosphatase
BMP-2: bone morphogenetic protein-2
RUNX2: runt-related transcription factor 2
OPN: osteopontin
DMEM: Dulbecco's modified Eagle's medium
PBS: phosphate-buffered saline
BV: bone volume
BMD: bone mineral density
BV/TV: bone volume fraction
Tb.N: trabecular number
Tb.Th: trabecular thickness
IOD: integral optical density
BMSC: bone marrow mesenchymal stem cell
MSC: mesenchymal stem cell
FCM: flow cytometry
HE: hematoxylin and eosin